

Method- and scheme-independent entropy production in turbulent kinetic simulations



Maxime Lesur*

Institut Jean Lamour, Université de Lorraine, 54506 Vandoeuvre-lès-Nancy Cedex, France
 Research Institute for Applied Mechanics, Kasuga, Kasuga Koen 6-1, 816-8580, Kyushu University, Japan

ARTICLE INFO

Article history:

Received 10 March 2015
 Received in revised form
 30 October 2015
 Accepted 4 December 2015
 Available online 11 December 2015

Keywords:

Ion-acoustic turbulence
 Vlasov code
 Collision operator
 Entropy

ABSTRACT

Numerical kinetic models of plasma turbulence require careful treatment of conserved quantities. In the collisionless limit, numerical dissipation can impact entropy in a non-controlled manner. In this paper, the impact of the error in entropy conservation is investigated. In a simulation of ion-acoustic turbulence, a large error (15%) in entropy conservation is found. Surprisingly, this error is independent of the numerical method, scheme, or number of grid points. Adding a collision operator resolves this issue, but only if the collision frequency is large enough that it modifies the qualitative time evolution of observables, such as electric field amplitude, anomalous resistivity, or phase-space structures.

© 2015 Elsevier B.V. All rights reserved.

For a wide range of astrophysical and laboratory plasma phenomena, collisions are negligible. Then, the evolution of the particle distribution in phase-space is usually described by the Vlasov equation, which translates the fact that the distribution is constant along particle orbits.

Accurate numerical simulation of collisionless plasmas requires careful treatment of conserved physical quantities, such as total mass, total energy and total entropy. For example, to obtain the turbulent steady-state accurately, spurious heating must be avoided. The numerical treatment of kinetic nonlinearities such as particle trapping is particularly challenging. Indeed, trapping involves the filamentation of phase-space (phase-space mixing), whereby an initially smooth particle distribution is mixed by the particle motion into very fine structures. Phase-space filaments eventually become smaller than the numerical grid size. Then information is inevitably lost, which breaks the conservation of entropy. This problem is well-known for Vlasov codes [1], but the impact on physics of interest, i.e. the evolution of coarse-grained observables, is unknown.

In overcoming the numerical issues associated with phase-space filamentation, one can distinguish three classes of approach. The first approach is to add a collision operator to the model [2], even if the collision frequency has to be artificially increased

to overcome the issues. The second approach is to add artificial filters [3] or damping [4] (it can be argued that Fourier codes [5] belong to this class). The third approach is to simply let numerical discretization replace collisions to dissipate the smallest scales and coarse-grain average the distribution function in an uncontrolled manner. For all three classes of approach, however, a concern is that simple models of collisions, numerical filtering, or numerical dissipation, are artificial, and may impact the physics of interest.

In this work, we report a systematic spurious entropy production, of 15% of the initial entropy, when the fully-nonlinear turbulent stage is reached, regardless of the numerical treatment. Indeed, the issue is not limited to Vlasov codes. The same error is found for fundamentally different types of simulation, i.e. Vlasov (semi-Lagrangian) and particle-in-cell (PIC), different schemes and different choices of grid sizes. This is shown in Fig. 1, which is the main figure in this paper, and which is discussed in detail in Section 3. Furthermore, the error is relatively insensitive to parameters of the physical system. As expected, a collision operator with velocity diffusion resolves the issue, but only if the collision frequency is so large that it dominates the long-time evolution.

1. Model

We restrict the analysis to a collisionless, one-dimensional, ion–electron plasma with an initial homogeneous current. We choose physical parameters such that the evolution of the plasma is dominated by ion-acoustic turbulence. Ion-acoustic waves [6,7] are longitudinal electrostatic waves, which are commonly observed in space and laboratory plasmas. The nonlinear saturation

* Correspondence to: Institut Jean Lamour, Université de Lorraine, 54506 Vandoeuvre-lès-Nancy Cedex, France.

E-mail address: maxime.lesur@polytechnique.org.

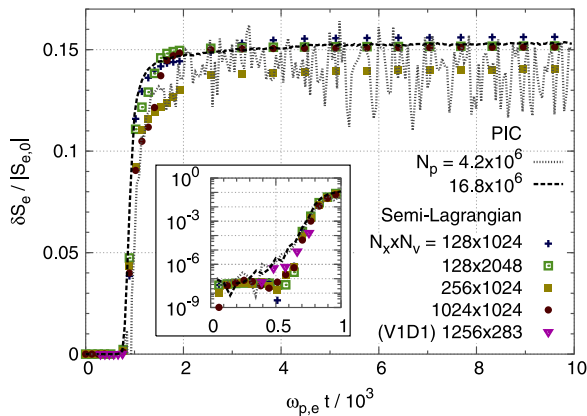


Fig. 1. Time-evolution of the perturbed electron entropy. Inset: zoom on the early stage, in semi-logarithmic scale. The simulation parameters are given in Section 1.4.

Table 1
Normalization.

Physical quantity	Normalization constant
Time	$\omega_{p,e}^{-1}$
Particle charge	e
Mass	m_e
Length	λ_D
Velocity	$v_{T,e}$
Distribution f	$n_0/v_{T,e}$
Electric field	$m_e v_{T,e}^2 / (e\lambda_D)$
Energy	$m_e v_{T,e}^2$

has been studied from the early 1960s [8–12]. Theory and experiments indicate that ion-acoustic waves are key agents of magnetic reconnection (via anomalous resistivity) [13–16], turbulent heating [17], particle acceleration [18], and play important roles in the context of laser–plasma interaction [19]. Furthermore, ion-acoustic waves constitute the basis for dominant fluctuations in magnetically confined plasmas. Indeed, drift-waves [20] arise from the ion-acoustic branch, modified by inhomogeneities and geometry effects. Linear instability of ion-acoustic waves requires that the velocity drift exceeds some finite threshold. However, nonlinear theory [21–23] predicts that ion-acoustic turbulence can grow nonlinearly, even for small drifts.

In the present work, we use a model of ion-acoustic turbulence as a paradigm for kinetic models in the presence of strong resonances.

1.1. Normalization

It is appropriate to normalize physical quantities with the constants listed in Table 1, where λ_D is the Debye length, $e = q_i = -q_e$ is the elementary charge, n_0 is the spatially-averaged plasma density, and m_s , $\omega_{p,s}$ and $v_{T,s} = (2T_s/m_s)^{1/2}$ are the mass, plasma frequency and thermal velocity, respectively, of species s ($s = i, e$).

1.2. Model description

The evolution of each particle distribution, $f_s(x, v, t)$ is given by the Vlasov equation,

$$\frac{\partial f_s}{\partial t} + v \frac{\partial f_s}{\partial x} + \frac{q_s E}{m_s} \frac{\partial f_s}{\partial v} = C(f_s), \quad (1)$$

where $C(f_s)$ is an eventual collision operator.

The evolution of the electric field $E(x, t)$ satisfies a current equation,

$$\frac{\partial E}{\partial t} = - \sum_s \frac{m_s \omega_{p,s}^2}{n_0 q_s} \int v f_s(x, v, t) dv. \quad (2)$$

Table 2
Relative error (order-of-magnitude) in energy and entropy conservation.

	Total energy	Entropy
Dissipative bump-on-tail	10^{-5}	10^{-5}
Ion-acoustic turbulence	10^{-3}	10^{-1}

The initial electric field is obtained by solving Poisson's equation. Analytically, satisfying Eqs. (1)–(2) at all times, if Poisson equation is satisfied at $t = 0$, is equivalent to satisfying Eq. (1) and Poisson equation at all times (given that the collision operator conserves particle number and momentum). Numerically, we have thoroughly checked that there is no significant discrepancy in the results between the method chosen in this work (solving Poisson at $t = 0$ and solving Eq. (2) at each time step), and a method that can seem more natural (i.e. solving Poisson at each time step).

The model is applicable as a statistical description of a plasma when electromagnetic perturbations are dominated by electrostatic waves in one direction. This is relevant for plasma immersed in a strong, relatively homogeneous magnetic field [24].

1.3. Numerical codes

To investigate the impact of the numerical method, and of the numerical scheme, we perform the same simulation with three different kinetic codes.

The first code is the semi-Lagrangian code COBBLES, which is based on the splitting method [3], and on the Constrained-Interpolation-Profile, Conservative Semi-Lagrangian (CIP-CSL) scheme [25]. In the CIP-CSL scheme, the evolution of space- and velocity-integrals of the distribution function is computed from separate kinetic equations, along with the evolution of the distribution function itself, in a way that keeps a flux balance between neighboring grids. The implementation guarantees the local conservation of density, up to the machine precision. COBBLES was described, verified, validated and benchmarked in Ref. [26] for a dissipative bump-on-tail (single species) model. COBBLES is capable of accurate long-time simulations, in various regimes, including chaotic ones [27,28], of the bump-on-tail instability in a one-species, 1D plasma. COBBLES was recently extended to treat two species kinetically. The extended code and its diagnostics are verified and benchmarked in the Appendix, by recovering several results of Ref. [12], including statistical properties of anomalous resistivity.

As a side note, and a general message in computational science, let us emphasize that the conservation properties strongly depend on the simulated physics. With the same COBBLES code, for two-species ion-acoustic turbulence, compared to one-species simulations of the dissipative bump-on-tail instability [29], the conservation of entropy and total energy is degraded by several orders of magnitude. Table 2 shows the order-of-magnitude of relative error in energy and entropy conservation for these two models for the same code (COBBLES).

The second code is the semi-Lagrangian code V1D1, which was developed at the British Antarctic Survey in Cambridge, originally by R.B. Horne and M.P. Freeman, and then further by C.E.J. Watt. V1D1 is based on the MacCormack method, which is an explicit finite difference method with predictor–corrector algorithm. It was used in many works, e.g. Refs. [30,12].

The third code is a simple PIC code, PICKLES (Particle-In-Cell Kinetic Lazy Electrostatic Solver), which is based on a fourth-order Runge–Kutta method. PICKLES can handle both full- f and δf treatments [23]. In this paper we use the δf version only. We denote the number of marker-particles per species as N_p .

1.4. Numerical simulations

Unless stated otherwise, and except in the appendix, we analyze a single physical system. The mass ratio is $m_i/m_e = 4$. The system

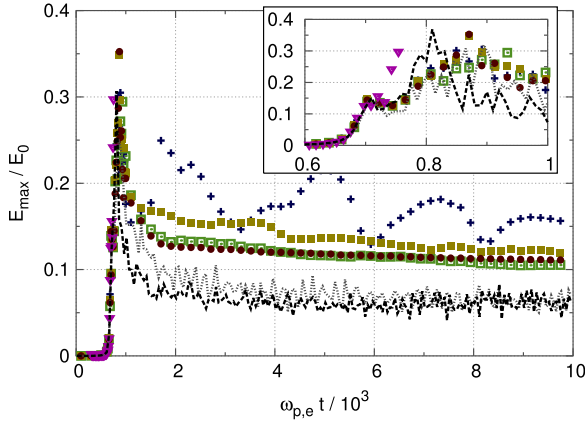


Fig. 2. Time-evolution of the electric field amplitude (moving time-average). Inset: zoom on the peak. The legend is shared with Fig. 1.

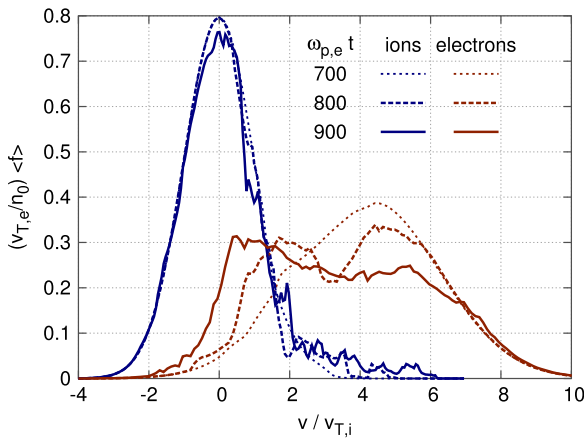


Fig. 3. Snapshots of velocity distributions.

size is $2\pi/k_1$, where $k_1 = 0.2$. The initial velocity distribution for each species is a Gaussian,

$$f_{0,s}(v) = \frac{n_0}{(2\pi)^{1/2} v_{T,s}} \exp\left(-\frac{(v - v_{0,s})^2}{2v_{T,s}^2}\right) \quad (3)$$

with $v_{0,i} = 0$ and $v_{0,e} = 2.1$ (slightly above linear instability threshold). The ion and electron temperatures are equal ($v_{T,i} = 0.5$). Boundary conditions are periodic in real space, and the implementation ensures zero-particle flux at the velocity cut-offs $v_{0,s} \pm v_{\text{cut},s}$, with $v_{\text{cut},i} = 3.5$ and $v_{\text{cut},e} = 7$, in order to avoid spurious leakage of particles [26].

Firstly, the collision operator in Eq. (1) is disabled. Thus, numerical discretization replaces collisions to dissipate the smallest scales and coarse-grain average the distribution function.

The only varying parameters, among the simulations presented in the next section, are the numerical scheme (semi-Lagrangian or PIC), the numerical method (CIP–CSL, MacCormack, or fourth-order Runge–Kutta), or the number of grid points or particles.

For COBBLES and V1D1, the numbers of grid points in configuration-space and velocity-space are denoted as N_x and N_v , respectively. For COBBLES, the time-step width is adaptive, with a maximum $\Delta t = 0.1$. As the electric field amplitude grows, the time-step width is halved before the Courant–Friedrichs–Lewy condition is violated. For PICKLES, the number of particles is denoted as N_p .

2. Evolution

Fig. 2 shows the time-evolution of the electric field amplitude, $E_{\text{max}}(t) \equiv \max_x [E(x, t)]$. All codes are in quantitative agreement

throughout the linear ($t < 0.57 \times 10^3$), and early-nonlinear stages ($0.57 \times 10^3 < t < 0.75 \times 10^3$) of the evolution.

At $t \approx 0.75 \times 10^3$, the V1D1 simulation diverges. Increasing the number of grids, the velocity cut-offs, or decreasing the time-step width does not solve this numerical issue, but rather only slightly postpones the time of divergence.

The other simulations are in qualitative agreement throughout the long-time nonlinear evolution. However, the PICKLES simulations underestimate the saturated amplitude. Indeed, the error in total energy conservation is of the order of 1% for PICKLES, and less than 0.1% for COBBLES.

Snapshots of the velocity distributions are shown in Fig. 3 for the COBBLES simulation for $N_x \times N_v = 1024 \times 1024$. This figure shows that most of the redistribution of electrons occurs between $t \approx 0.7 \times 10^3$ and $t \approx 0.9 \times 10^3$.

3. Entropy production

Let us now focus on the entropy. Numerically, it is estimated as

$$S(t_n) = - \sum_{i=1}^{N_x} \sum_{j=1}^{N_v/2} (f_{i,j}^n \log f_{i,j}^n + f_{i,N_v+1-j}^n \log f_{i,N_v+1-j}^n) \Delta x \Delta v. \quad (4)$$

3.1. Collisionless limit

In the absence of a collision operator, entropy is trivially conserved in the physical (continuous) model. In the numerical simulation, we measure the error $\delta S \equiv S(t) - S_0$, where $S_0 \equiv S(t = 0)$. Fig. 1 shows the time-evolution of the error in electron entropy conservation, in COBBLES for four different numbers of grid points, in V1D1, and in PICKLES, for two different numbers of particles. The error in total electron entropy conservation is negligible until $t \approx 0.7 \times 10^3$. Then, it quickly increases to 15%. This entropy production is remarkably insensitive to the numerical treatment. The order-of-magnitude of the error is the same for PIC or Vlasov codes, for CIP–CSL or MacCormack schemes, for different numbers of grid points, for different numbers of particles, and for widely different time-step widths (not shown here).

In the case of COBBLES, we also investigated the impact of velocity cut-offs, but found no impact, as long as v_{cut} was large enough. In the COBBLES simulations discussed in this paper, the cut-offs are such that the distribution function at the cut-offs is typically between 10^{-25} and 10^{-20} (normalized to its peak). Doubling the cut-off velocity (along with N_v) did not have any impact that could be distinguished from fluctuations due to random phases of initial perturbation.

Fig. 4 shows how the entropy conservation error depends on three physical parameters, the initial velocity drift $v_d \equiv v_{0,e} - v_{0,i}$, the mass ratio $m_r \equiv m_i/m_e$, and the system size as defined by k_1 . The velocity drift is normalized by the critical value for linear instability, $v_{d,\text{cr}} = 1.96$ for $m_r = 4$, and $v_{d,\text{cr}} = 3.93$ for $m_r = 25$. Although the error in entropy conservation decreases as linear marginality is approached, it saturates to a large value, of the order of 10%. The problem is slightly worse for larger system size, and slightly milder for larger mass ratio, but the error stays within the same order of magnitude.

3.2. Impact of collision operator

As expected, the entropy balance can be recovered by including a collision operator that efficiently dissipates small scale structures. However, our simulations suggest that the error in entropy balance stays within the same order of magnitude as in the collisionless case, unless collision frequency is so large that it modifies the qualitative behavior of observables, such as the electric field.

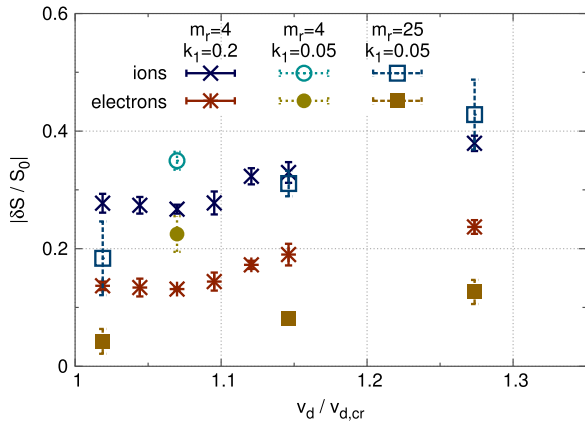


Fig. 4. Peak relative entropy conservation error, as a function of the initial velocity drift $v_d \equiv v_{0,e} - v_{0,i}$, normalized by the linear instability threshold $v_{d,cr}$. The error bars correspond to standard deviations, each based on four simulations with different numbers of grid points.

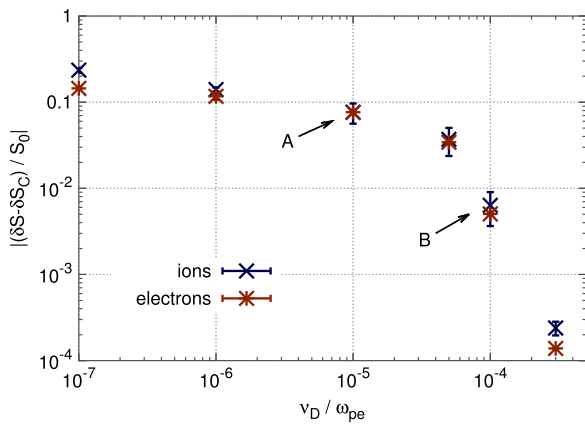


Fig. 5. Peak relative error in entropy balance, as a function of the collision frequency. The simulation parameters are the same as in Figs. 1–3, except for the presence of collisions.

We now include a velocity diffusive collision operator,

$$C(f_s) = v_{D,s} \frac{\partial^2 (f_s - f_{0,s})}{\partial v^2}, \quad (5)$$

where $v_D \equiv v_{D,e}$ is a free parameter, and $v_{D,i} = v_{D,e} (m_e/m_i)^{1/2}$. In this case, the continuous system satisfies an entropy balance for each species,

$$\frac{d\delta S}{dt} = \frac{d\delta S_C}{dt} \equiv - \int v_{D,s} \frac{\partial^2 (f - f_0)}{\partial v^2} \log f \, dx \, dv. \quad (6)$$

In the simulations, we measure the time integral $\delta S - \delta S_C$ (in order to have a measure with the same dimension as above). Then we define the error in entropy balance as $(\delta S - \delta S_C)/S_0$. Fig. 5 shows how the error in entropy balance varies as a function of the collision frequency v_D . The error decreases dramatically with increasing collision frequency. At $v_D/\omega_{p,e} = 5 \times 10^{-5}$, it is one order-of-magnitude lower than in the collisionless limit. However, for such a value of collision frequency, the time-evolution, and steady-state value of electric field are significantly changed, and sensitive to the collision frequency. This can be seen in Fig. 6, which compares the time-evolution of electric field for different collision frequencies. Similar conclusions were obtained for the anomalous resistivity with the same threshold in v_D .

The collision frequency $v_D/\omega_{p,e} = 10^{-5}$ corresponds in order-of-magnitude to rather dense parts of the interplanetary medium, with e.g. density 10^3 cm^{-3} and temperature 200 K. If one were

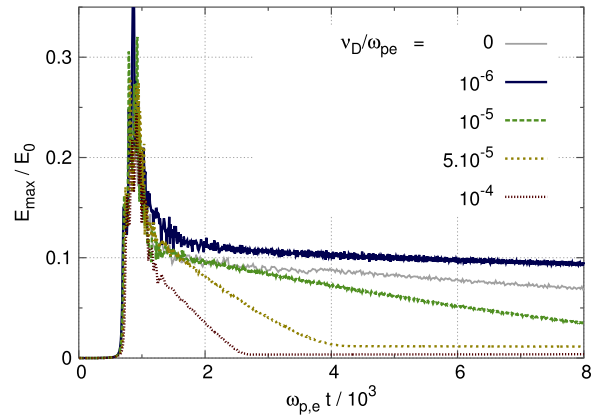


Fig. 6. Time-evolution of the electric field amplitude for different values of the velocity-diffusion collision frequency.

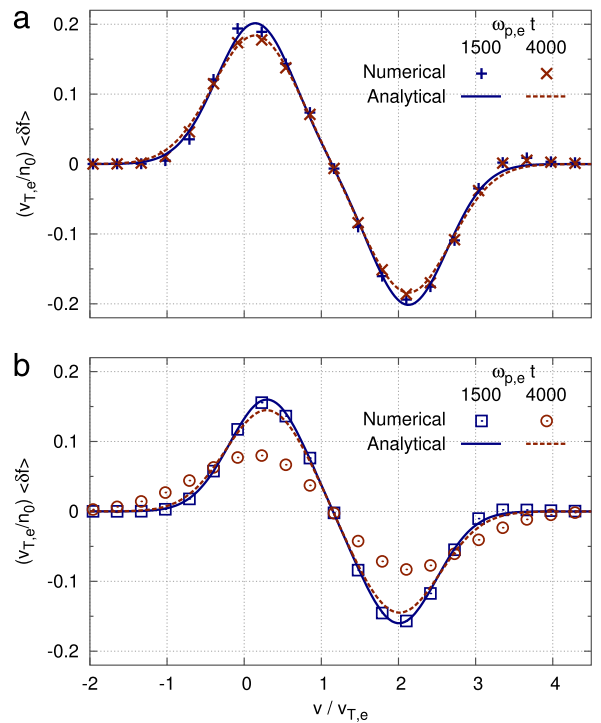


Fig. 7. Perturbation in electron velocity distribution. (a) Simulation A. (b) Simulation B. Solid curves: initial fit, Eq. (7). Dashed curves: analytical solution, Eq. (8), of diffusion equation from initial fit.

to model ion-acoustic turbulence in such a plasma with a kinetic numerical simulation, one could perform a first simulation, simulation A, with a collision frequency calculated from equilibrium plasma parameters, $v_D/\omega_{p,e} = 10^{-5}$. As suggested by the present work, one would then be confronted with a spurious entropy production of about 10%. One could then try to artificially increase the collision frequency in a second simulation, simulation B, to e.g. $v_D/\omega_{p,e} = 10^{-4}$, even though the target plasma still has a collisionality $v_D/\omega_{p,e} = 10^{-5}$. Spurious entropy production in simulation B would then be reduced to less than 1%. Let us then address the following question: which simulation, A or B (as indicated by arrows in Fig. 5), better represents the target analytical model, that is Eqs. (1), (2) and (5) with $v_D/\omega_{p,e} = 10^{-5}$. Fig. 7 compares snapshots of the perturbation in electron velocity distribution, $\langle \delta f_e \rangle = \langle f_e \rangle_x - f_{0,e}$, in simulations A and B. At $t = t_0 \equiv 1500 \omega_{p,e}^{-1}$, both

simulations feature a BGK-like flattening, which can be fitted as

$$\langle \delta f_e \rangle (t_0) = a_0 \exp \left[- \left(\frac{v - v_1}{u_0} \right)^2 \right] - a_0 \exp \left[- \left(\frac{v - v_2}{u_0} \right)^2 \right]. \quad (7)$$

Between $t = t_0$ and a later time $t = t_1 \equiv 4000\omega_{p,e}^{-1}$, the spatially-averaged evolution of the BGK-like structure is dominated by collisional diffusion [31]. Therefore, the electron velocity distribution approximately follows

$$\langle \delta f_e \rangle (t) = a(t) \exp \left[- \left(\frac{v - v_1}{u(t)} \right)^2 \right] - a(t) \exp \left[- \left(\frac{v - v_2}{u(t)} \right)^2 \right], \quad (8)$$

with $a(t) = a_0[1 + 4v_D(t - t_0)/u_0^2]^{-1/2}$ and $u(t) = [u_0^2 + 4v_D(t - t_0)]^{1/2}$. The analytical prediction for the velocity distribution of the BGK-like structure at $t = t_1$ is shown as dashed curves in Fig. 7, for $v_D/\omega_{p,e} = 10^{-5}$ (corresponding to the target analytical model). We observe that simulation A is in quantitative agreement with this analytical prediction, but not simulation B. Of course, the result of simulation B would be in quantitative agreement with the analytical prediction if we had chosen $v_D/\omega_{p,e} = 10^{-4}$. However, that is not our target value for the analytical model, but rather the value to which we artificially increased collision frequency in numerical simulation B in order to mitigate the spurious entropy production problem.

At least from the point-of-view of the evolution of phase-space structures, there are regimes where the analytical solution is closer to numerical simulations with large entropy balance error, than to numerical simulations with small entropy balance error but artificially large collision frequency. Therefore, artificially increasing collision frequency may not be a suitable solution to the entropy problem in general.

4. Discussion

The spurious entropy production is surprisingly insensitive to the numerical treatment, and occurs during particle redistribution. This suggests that the error is due to the generation of small scales during redistribution, and that, while the diffusion mechanism is artificial, the magnitude of the entropy source is representative of physical dissipative processes. Similar observations and conclusions were obtained for numerical models of the atmospheric climate system [32].

Particle redistribution is known to be associated with the formation of self-trapped structures in phase-space [23,33], with various sizes. These structures are measured by the phasestrophy [34], which is related to entropy. Entropy production may be related to the production of phase-space structures, which are too small to be resolved with any reasonable number of grid points.

5. Conclusions

In the fully-nonlinear stage of collisionless ion-acoustic turbulence, a spurious, $\sim 10\%$ entropy production was observed, regardless of the numerical treatment, and relatively insensitive to the parameters of the physical system. One hypothetical explanation is that the entropy production is a measure of a physical (as opposed to numerical) process, namely the creation of structures with scales much smaller than reasonably accurate grids.

The above analysis suggests that there are regimes where accuracy of entropy conservation is not a good measure of the accuracy of the time-evolution of most coarse-grain observables such as density, temperature, electromagnetic fields, anomalous resistivity, or phase-space structures.

Acknowledgments

The authors are grateful for stimulating discussions with participants in the Festival de Théorie. This work was supported by grants-in-aid for scientific research of JSPS, Japan (21224014, 23244113, 25887041, and 15K18305), and by the collaboration program of the RIAM of Kyushu University and Asada Science Foundation. Computations were performed on the XT and SX systems in Kyushu University, and on the Asterix system in Lorraine University.

Appendix. CIP-CSL simulation of 2-species plasma

In this paper, the CIP-CSL scheme was applied for the first time to ion-acoustic turbulence. In practice, this work consists of an extension of the single-species code COBBLES to 2 species. Although this extension may seem like a trivial task, it actually required several key improvements, such as the use of the in-pairs summation method, and computing the current not from the distribution function f , but from the perturbed, velocity-integrated distribution function $\delta\sigma_v$. These improvements were necessary because fully-nonlinear simulations of ion-acoustic turbulence are much more stringent than those of single-mode Langmuir wave, especially for real mass ratio. Therefore careful verification and benchmarks are necessary steps before exploiting the code for investigating new physics of ion-acoustic turbulence. These verifications and benchmarks are described below.

A.1. Numerical scheme

The variables are sampled on a uniform Eulerian grid (x_i, v_j) , where $i = 1 \dots N_x$ and $j = 1 \dots N_v$. $f_{i,j}^n$ is the value of the distribution f at the grid point of coordinates $x_i = i \Delta x$, $v_j = -v_{\text{cut}} + j \Delta v$ at the time $t_n = n \Delta t$. The density within a cell and the line densities are defined as,

$$\rho_{i,j}^n = \int_{x_i}^{x_{i+1}} \int_{v_j}^{v_{j+1}} \tilde{f}^n(x, v) dx dv, \quad (A.1)$$

$$\sigma_{x_{i,j}}^n = \int_{x_i}^{x_{i+1}} \tilde{f}^n(x, v_j) dx, \quad (A.2)$$

$$\sigma_{v_{i,j}}^n = \int_{v_j}^{v_{j+1}} \tilde{f}^n(x_i, v) dv. \quad (A.3)$$

The evolution of electric field, Eq. (2), is treated by a forward Euler scheme, or, alternatively, by solving Poisson equation at each time-step in Fourier space. When the current equation is used, we found that the inaccuracy in total energy conservation is reduced by evaluating the current from $\delta\sigma_v = \sigma_v(t) - \sigma_v(t = 0)$ instead of from $f(t)$.

A.2. Parameters

Hereafter, we adopt the physical parameters of Ref. [12]. The mass ratio is $m_i/m_e = 25$. The system size is $2\pi/k_1$, where $k_1 = 0.0147$. The electron mean velocity is $v_{0,e} = 1.2\sqrt{2} = 1.70$ (note that the present definition of thermal velocity differs from

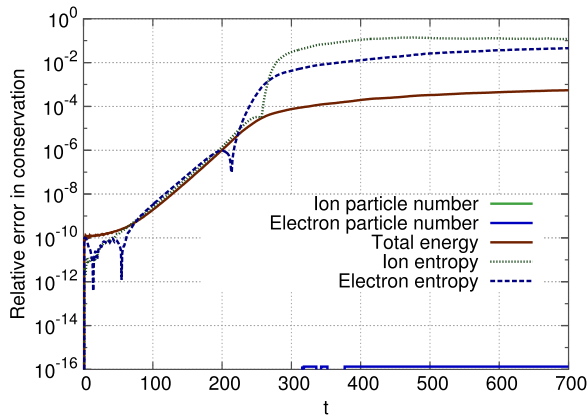


Fig. A.8. Absolute value of relative error in particle number, total energy and entropy conservation.

the reference by a factor $\sqrt{2}$). The temperature ratio is $T_e/T_i = 2$ ($v_{T,i} = 0.141$). The initial velocity distributions are shown in Fig. A.12. The velocity cut-offs are $\pm v_{\text{cut},s}$, with $v_{\text{cut},i} = 2.87$ and $v_{\text{cut},e} = 10.2$. The initial electron distribution is perturbed as

$$f_e = \left[1 + \sum_{n=1}^{n_{\text{max}}} k_n \epsilon \cos(k_n x + \phi_n) \right] f_{0,e}(v), \quad (\text{A.4})$$

where $k_n = nk_1$, $n_{\text{max}} = 53$ ($k_{\text{max}} = 0.78$), ϕ_n is a random phase, and $\epsilon = 6.76 \times 10^{-5}$, which corresponds to a thermal fluctuation level.

A.3. Conservation properties

In the numerical simulation, velocity-integrals are calculated using the in-pairs method. The total number of particles, or equivalently, total mass, is obtained as

$$N(t_n) = \sum_{i=1}^{N_x} \sum_{j=1}^{N_v/2} (\rho_{i,j}^n + \rho_{i,N_v+1-j}^n). \quad (\text{A.5})$$

The total energy is given by $H = T_i + T_e + W$, where T is the kinetic energy,

$$T(t_n) = \frac{m}{2} \sum_{i=1}^{N_x} \sum_{j=1}^{N_v/2} (v_j^2 f_{i,j}^n + v_{N_v+1-j}^2 f_{i,N_v+1-j}^n) \Delta x \Delta v, \quad (\text{A.6})$$

and W is the electric-field energy,

$$W(t_n) = \frac{1}{2} \sum_{i=1}^{N_x} E^2(x_i, t_n) \Delta x. \quad (\text{A.7})$$

In the above definitions, we dropped the species subscript s .

Fig. A.8 shows the absolute value of relative error in particle number and energy (e.g. $|\delta N|/N(0)$, where $\delta N \equiv N(t) - N(0)$) in a simulation with $N_x = 1024$ and $N_v = 2048$ grid points. This computation, which extends to $t = 2000$ (not shown here) took 4 real-world hours on 64 parallel processors, using Cray XT4 system. The relative error in total mass conservation is equal to the machine precision ($10^{-14}\%$). The relative error in total energy is below 0.1%.

Fig. A.9 shows the relation between kinetic energy and field energy. Note that the field energy is much smaller than the variation of kinetic energy of any one species. Thus in terms of field energy only, the energy conservation is relatively inaccurate, $|\delta H|/W(t) \sim 0.5$, since in this point-of-view the field energy is compared to the small difference between $|\delta T_i|$ and $|\delta T_e|$. We also checked convergence, that is the error for each conserved quantity decreases with increasing grid points and decreasing time-step width. Similar results were obtained with simulations where Poisson equation is solved at each time-step instead of Eq. (2).

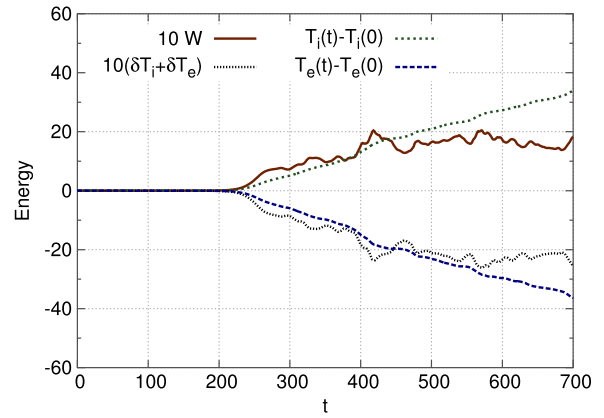


Fig. A.9. Energy balance. Field energy and variation of total kinetic energy, both magnified 10 times, as well as variation in kinetic energy for each species.

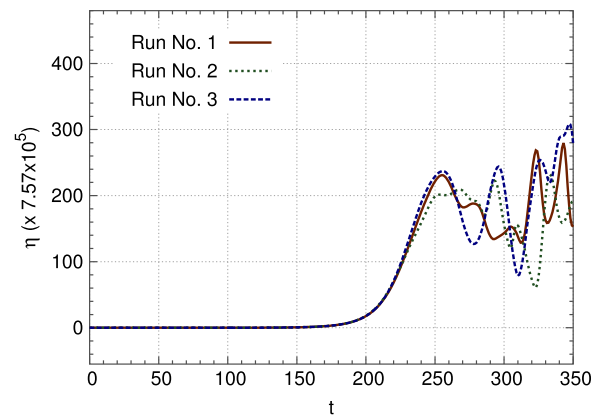


Fig. A.10. Time-series of anomalous resistivity, for 3 different sets of initial random phases. The vertical axis is normalized to allow direct comparison with Fig. 1(a) of Ref. [12].

A.4. Benchmark

We benchmark the two-species extension of the COBBLES code by reproducing results of Ref. [12], which were obtained from the V1D1 code, for both small and large mass ratios.

A.4.1. Small mass ratio

We ran 128 simulations with different sets of initial random phases ϕ_n . Fig. A.10 shows the evolution of anomalous resistivity for three of these runs. The vertical axis is multiplied by a factor such that the value can be read directly as the value of resistivity in units of Ωm for the plasma parameters of the reference. There is a good qualitative agreement with the reference. Although the fluctuations in the final stage seem smaller than in the reference, we will see that statistically this is not the case. Here, anomalous resistivity η is defined in a way which is more general but slightly different than the reference,

$$(p_i - p_e) \eta = E_0 - \frac{m_i}{m_i + m_e} \frac{d(p_i - p_e)}{dt}, \quad (\text{A.8})$$

where E_0 is the spatial average of the electric field, and $p_s \equiv \int v f_s dx dv$ is the momentum of species s . However, since $E_0 = 0$, the definitions differ only by a factor $1/(1 + m_e/m_i) = 0.96$ in this case.

Fig. A.11 shows the evolution of the fastest linearly growing mode for the three same runs. Similarly, the vertical axis is multiplied by a factor such that the value can be read directly as the value of E_k in units of Vm^{-1} for the plasma parameters of the

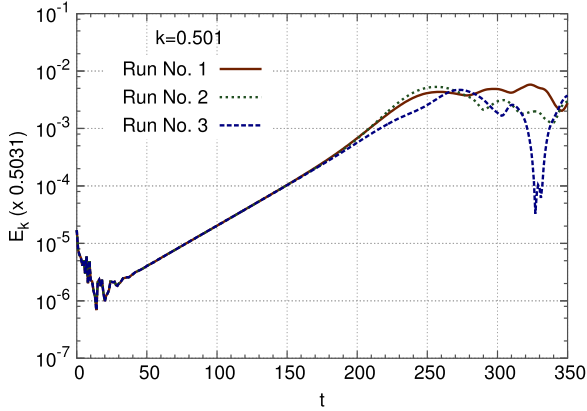


Fig. A.11. Time-series of Fourier component $k = 0.501$ of the electric field. The vertical axis is normalized to allow direct comparison with Fig. 1(b) of Ref. [12].

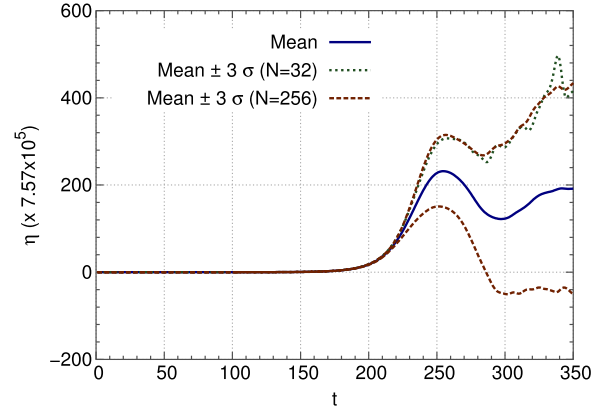


Fig. A.14. Mean value and $\pm 3\sigma$ curves, for ensembles of 32 and 128 runs. The vertical axis is normalized to allow direct comparison with Fig. 4(b) of Ref. [12].

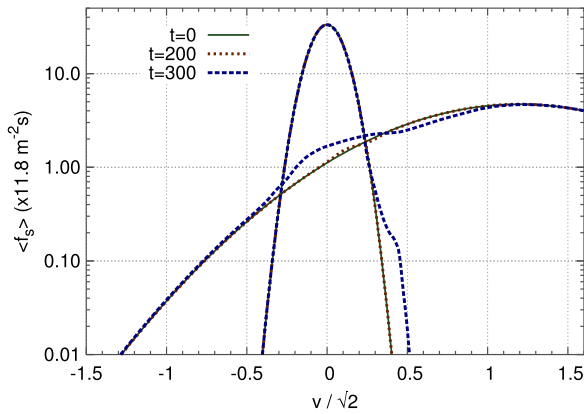


Fig. A.12. Snapshots of velocity distributions. The axes are normalized to allow direct comparison with Fig. 1(c) of Ref. [12].

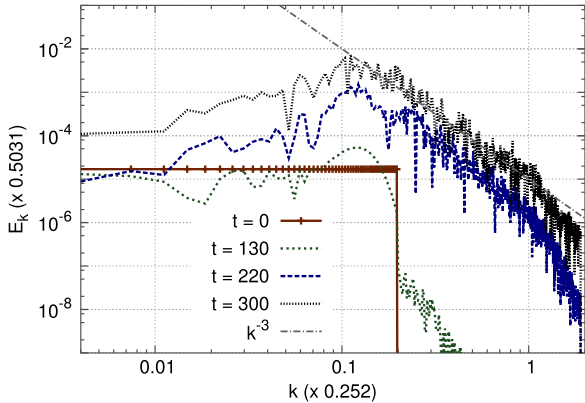


Fig. A.13. Snapshots of electric field spectrum in k -space. The axes are normalized to allow direct comparison with Fig. 2 of Ref. [12].

reference. The linear growth rate is recovered, saturation occurs at a similar time (between $t = 200$ and $t = 250$), and the value at $t = 350$ agrees with the one run shown in the reference.

Fig. A.12 shows snapshots of the velocity distributions (spatial averages of f_s). Again, one can compare directly the latter figure with the reference, and observe a good quantitative agreement, for example for the size of the plateau.

Fig. A.13 shows snapshots of electric field spectrum in k -space, at four different times. Again, one can compare directly the latter figure with the reference. Although the initial conditions are slightly different for $k > k_{\max}$, the spectrum reproduces the evolution observed in the reference. Many features, such as a broad

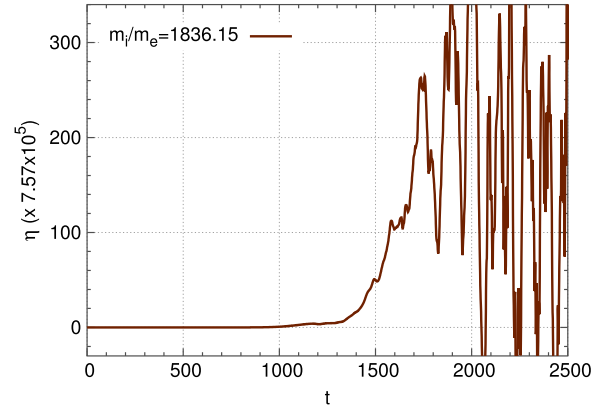


Fig. A.15. Time-series of anomalous resistivity, for real mass ratio. The vertical axis is normalized to allow direct comparison with Fig. 8(a) of Ref. [12].

pick around $k = 0.1$ at $t = 130$, or a $E_k \sim k^{-3}$ law for high k at $t = 300$, are in agreement with the reference. This comparison is important to ensure that the field equation is accurately treated.

Reproducing fully-nonlinear, turbulent time-evolution is a stringent test for a numerical code. However, meaningful quantitative benchmark requires statistical analysis. Fig. A.14 shows the average $\bar{\eta}$ of the anomalous resistivity, as well as $\bar{\eta} \pm 3\sigma$ curves, where σ is the standard deviation, for an ensemble of 128 runs. There is a satisfying quantitative agreement with the reference, although we obtain a larger standard deviation, up to 40% higher than the reference. To show that the average and the standard deviation converged, a $\bar{\eta} + 3\sigma$ curve, obtained for an ensemble of 32 runs, is super-imposed.

In the reference, the skewness and kurtosis of the probability distribution of η are also calculated. However, 128 is not a high enough number of ensemble for skewness and kurtosis to converge in the present series of simulations.

A.4.2. Real mass ratio

In this subsection, we benchmark simulations with real ion–electron mass ratio. We adopt the parameters of Table 2 in Ref. [12]. The mass ratio is $m_i/m_e = 1836.15$, the system size is $2\pi/k_1$, where $k_1 = 0.0197$. The electron drift velocity is $v_{0,e} = 1.70$. The temperature ratio is $T_e/T_i = 2$ ($v_{T,i} = 0.0165$). The velocity cut-offs are $v_{\text{cut},i} = 0.358$ and $v_{\text{cut},e} = 10.2$. The parameters of initial electron distribution are $n_{\max} = 43$ ($k_{\max} = 0.847$), and $\epsilon = 6.76 \times 10^{-5}$. The grid points numbers are $N_x = 1024$ and $N_y = 4096$.

Fig. A.15 shows the evolution of anomalous resistivity. There is a good qualitative agreement with the reference. Unfortunately, the

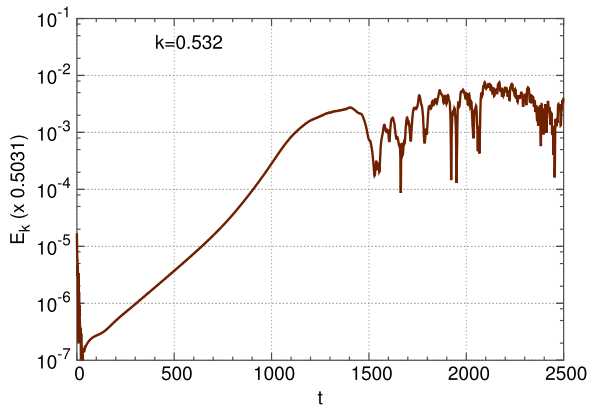


Fig. A.16. Time-series of Fourier component $k = 0.532$ of the electric field for real mass ratio. The vertical axis is normalized to allow direct comparison with Fig. 8(b) of Ref. [12].

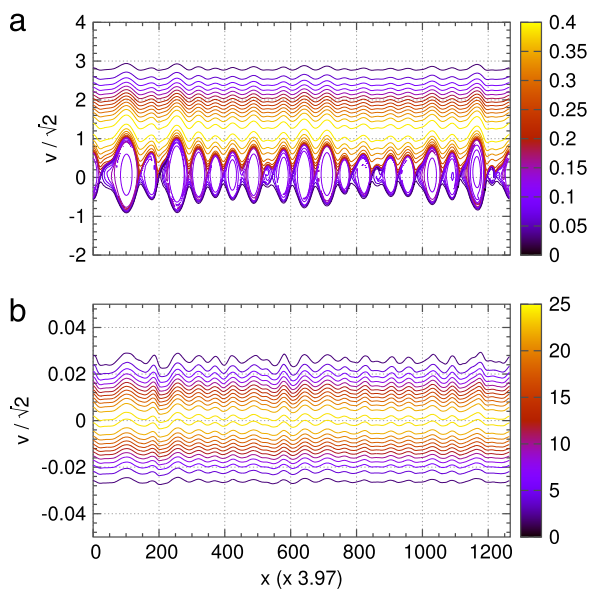


Fig. A.17. Snapshot of distribution functions, at $t = 1600$, for real mass ratio. (a) Electron distribution. (b) Ion distribution. The axes are normalized to allow direct comparison with Fig. 9 of Ref. [12], except for the color code. (For interpretation of the references to colour in this figure legend, the reader is referred to the web version of this article.)

reference does not include statistical investigation of anomalous resistivity.

Fig. A.16 shows the evolution of the fastest linearly growing mode. The linear growth rate is recovered, saturation occurs at a

similar time (between $t = 1100$ and $t = 1200$), and the saturated value is $10^{-3} < E_k < 10^{-2}$, in agreement with the reference.

Fig. A.17 shows a snapshot of electron and ion distribution functions at $t = 1600$. Many features coincide with the distribution shown in Fig. 9(b) and (d) in the reference, namely the electron island sizes $\Delta v/\sqrt{2}$ from 0.3 to 2 and $3.97\Delta x$ from 50 to 100, the merging process e.g. around $3.97x = 100$, and the absence of island in the ion distribution.

References

- [1] A.J. Klimas, *J. Comput. Phys.* 68 (1) (1987) 202–226.
- [2] F. Grant, M. Feix, *Phys. Fluids* 10 (4) (1967) 696–702.
- [3] C.Z. Cheng, G. Knorr, *J. Comput. Phys.* 22 (3) (1976) 330–351.
- [4] G. Joyce, G. Knorr, H.K. Meier, *J. Comput. Phys.* 8 (1) (1971) 53–63.
- [5] G. Knorr, *Z. Naturforsch* 18a (1963) 1304.
- [6] L. Tonks, I. Langmuir, *Phys. Rev.* 33 (1929) 195–210.
- [7] R.W. Revans, *Phys. Rev.* 44 (1933) 798–802.
- [8] V. Petviashvili, *Dokl. Akad. Nauk SSSR* 153 (6) (1963) 1295.
- [9] B. Kadomtsev, *Voprosy Teorii Plazmy*, vol. 4, Gosatomizdat, Moscow, 1964, p. 188.
- [10] R. Sagdeev, A. Galeev, *Nonlinear Plasma Theory*, W.A. Benjamin, New York, 1969.
- [11] A. Galeev, R. Sagdeev, *Voprosy Teorii Plazmy*, vol. 7, Atomizdat, Moscow, 1973, p. 205.
- [12] P. Petkaki, M.P. Freeman, T. Kirk, C.E.J. Watt, R.B. Horne, *J. Geophys. Res.* 111 (A10) (2006) 1205.
- [13] R. Sagdeev, *Proceedings of Symposia in Applied Mathematics*, American Mathematical Society, Providence, RI, 1967.
- [14] F.V. Coroniti, A. Eviatar, *Astrophys. J. Suppl. Series* 33 (1977) 189–210.
- [15] A.A. Galeev, R.Z. Sagdeev, in: A.A. Galeev, R.N. Sudan (Eds.), *Basic Plasma Physics: Selected Chapters*, in: *Handbook of Plasma Physics*, vol. 1, 1984, p. 271.
- [16] J. Labelle, R. Treumann, *Space Sci. Rev.* 47 (1–2) (1988) 175–202.
- [17] S.Q. Mah, H.M. Skarsgard, A.R. Strilchuk, *Phys. Rev. Lett.* 25 (1970) 1409–1413.
- [18] G.-P. Wu, G.-L. Huang, Y.-H. Tang, *Chinese J. Astr. Astrophys.* 5 (2005) 99–109.
- [19] W.L. Kruer, *The Physics of Laser Plasma Interactions*, in: *Frontiers in Physics*, vol. 73, Addison-Wesley Publishing Co, Reading, MA, 1988.
- [20] B. Kadomtsev, O. Pogutse, *Nucl. Fusion* 11 (1) (1971) 67.
- [21] T.H. Dupree, *Bull. Am. Phys. Soc.* 26 (1981) 1060.
- [22] T.H. Dupree, *Phys. Fluids* 26 (9) (1983) 2460–2481.
- [23] M. Lesur, P. Diamond, Y. Kosuga, *Plasma Phys. Control. Fusion* 56 (7) (2014) 075005.
- [24] M.M. Oppenheim, G. Vetoulis, D.L. Newman, M.V. Goldman, *Geophys. Rev. Lett.* 28 (9) (2001) 1891–1894.
- [25] T. Nakamura, R. Tanaka, T. Yabe, K. Takizawa, *J. Comput. Phys.* 174 (1) (2001) 171–207.
- [26] M. Lesur, Y. Idomura, X. Garbet, *Phys. Plasmas* 16 (9) (2009) 092305.
- [27] M. Lesur, Y. Idomura, K. Shinohara, X. Garbet, the JT-60 Team, *Phys. Plasmas* 17 (12) (2010) 122311.
- [28] M. Lesur, Y. Idomura, *Nucl. Fusion* 52 (9) (2012) 094004.
- [29] M. Lesur, *The berk-breizman model as a paradigm for energetic particle-driven Alfvén eigenmodes* (Ph.D. thesis), Ecole Polytechnique, France, 2011.
- [30] C.E.J. Watt, R.B. Horne, M.P. Freeman, *Geophys. Rev. Lett.* 29 (1) (2002) 4–1–4–4.
- [31] M. Lesur, *Phys. Plasmas* 20 (5) (2013) 055905.
- [32] T. Woollings, J. Thuburn, Q. J. R. Meteorol. Soc. 132 (614) (2006) 43–59.
- [33] M. Lesur, P.H. Diamond, Y. Kosuga, *Phys. Plasmas* 21 (11) (2014) 112307.
- [34] M. Lesur, P.H. Diamond, *Phys. Rev. E* 87 (2013) 031101.